J Mater Sci: Mater Electron (2017) 28:13209–13216
DOI 10.1007/s10854-017-7156-3

NO_2 sensing studies of bio-green synthesized Au-doped SnO_2

Ketan P. Gattu[1] · Anil A. Kashale[1] · Kalyani Ghule[1] · Vijay H. Ingole[1] · Ramphal Sharma[1] · Nishad G. Deshpande[2] · Anil V. Ghule[1,3]

Received: 2 March 2017 / Accepted: 15 May 2017 / Published online: 19 May 2017

Abstract Gold (Au) doped SnO_2 nanoparticles have been synthesized using remnant water (ideally kitchen waste) collected from soaked Bengal gram beans (*Cicer arietinum* L.) extract. The synthesized nanoparticles were initially investigated for their structural, morphological and vibrational properties. The structural properties revealed rutile structure with narrow size distribution and average crystallite size of ~25 nm. The investigation using UV–Vis spectroscopy, and Raman spectroscopy indicated the formation of structural defects and oxygen vacancies due to bio-green synthesis and incorporation of Au in SnO_2 lattice. Subsequently, Au-doped biosynthesized SnO_2 nanoparticles were coated onto the glass substrate using doctor blade method to form thin films. These thin films were investigated for their gas sensing properties and were found to be highly sensitive to NO_2 at 200 °C operating temperature. The reported gas sensing results suggest that the biosynthesis of Au-doped SnO_2 is a promising method to fabricate low-cost SnO_2 based NO_2 sensor.

Electronic supplementary material The online version of this article (doi:10.1007/s10854-017-7156-3) contains supplementary material, which is available to authorized users.

✉ Anil V. Ghule
anighule@gmail.com

[1] Department of Nanotechnology, Dr. Babasaheb Ambedkar Marathwada University, Aurangabad, Maharashtra, India

[2] Department of Physics, Shivaji University, Kolhapur, India

[3] Green Nanotechnology Laboratory, Department of Chemistry, Shivaji University, Kolhapur, India

1 Introduction

Nitrogen dioxide (NO_2) gas is well known as an irritant gas, it is an intermediate product of the industrial synthesis of nitric acid. The most prominent and common sources of human exposure to NO_2 gas are combustion engines, burning fossil fuels, cigarette smoke, butane and kerosene heaters and stoves [1]. NO_2 can cause respiratory infections, photochemical smog, acid rain [2] and it is harmful to human health and life. Exposure to unsafe higher levels can cause severe reactions for people with underlying pulmonary diseases like chronic obstructive pulmonary disease or asthma [3]. NO_2 reacts with water droplets in the trachea and lungs forming droplets of nitric acid. These tiny droplets of nitric acid penetrate deep into the lungs causing various respiratory diseases [3]. NO_2 exposure has also being associated with sudden infant death syndrome [4]. Thus, it is imperative to develop a sensor for detecting NO_2 gas. Many solid state gas sensors have been recently explored for NO_2 gas sensing such as WO_3 [4], VO_2 [5], NiO [6], and SnO_2 [7]. Among these, SnO_2 as a gas sensor have been widely explored and thus most of the attention has been paid to the synthesis of nanostructured SnO_2 materials and tuning its properties for selectivity and sensitivity [8–10]. Studies have proved that the properties and performances of SnO_2-based devices are dramatically influenced by structural features [11, 12]. The introduction of noble metal dopants into the host system is one of the important methods to modify the material properties. Also, the noble metal gold (Au) is reported to reduce the activation energy (E_a) of the reaction between target molecules and ionosorbed oxygen species [13, 14], and thus has been widely used to enhance the sensing performance [15–18].

Thus, with a need for simple and economic SnO_2 gas sensor, here in this work, we present a sensor material of

Au-doped SnO_2 nanoparticle thin film biosynthesized by using remnant water (ideally kitchen waste) collected from soaked Bengal gram beans (*Cicer arietinum* L.). Here, the natural biomolecule present in the extract and responsible for biosynthesis is pectin. It is a complex polysaccharide that is present in most primary cell walls [19] and has the ability to bind some organic and inorganic materials via molecular interactions [20]. Furthermore, the gas sensing properties of biosynthesized Au-doped SnO_2 for NH_3, LPG, H_2S and NO_2 gasses were explored, wherein it showed the enhanced response for NO_2 gas. The concentration-dependent response of the sensor for NO_2 was also investigated for linearity.

2 Experimental

2.1 Synthesis of SnO_2 nanoparticles

Figure 1 shows the schematic for the bio-green synthesis of Au- doped SnO_2 nanoparticles. The synthesis procedure [21] consists of soaking 20 g dry Bengal gram beans (*C. arietinum* L.) in 100 mL of DI water for 6 h at room temperature. Thereafter, the soaked seeds were removed and the extract was filtrated using a glass-fiber filter (GF/F) to be free from particulate matter. 10 mL of aqueous $SnCl_4$ (0.01 M) solution was added to 10 mL of the gram bean extract and diluted to 50 mL. $HAuCl_4$ was used as a source of Au, an appropriate amount of $HAuCl_4$ (Sigma-Aldrich) was added to this solution for having 5 wt% Au doping. The solution was then centrifuged and the powder so obtained was calcined at 600 °C to remove the organic contaminants. This powder was then thoroughly mixed with polyethylene glycol as a binder and coated onto the precleaned glass substrates to form thin films using the doctor blade method. The coated thin films were then dried at room temperature and calcined at 450 °C in air for 1 h to remove the binder and were used for further characterization and gas sensing application.

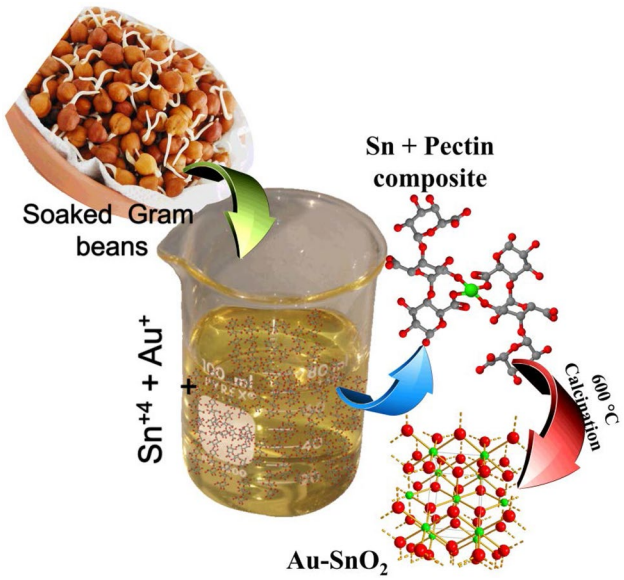

Fig. 1 Schematic of synthesis of Au-doped SnO_2

2.2 Characterization details

XRD patterns of both pure and Au-doped samples were recorded using Rigaku Miniflex X-ray diffractometer equipped with intense $CuK\alpha_1$ radiation ($\lambda = 1.54$ Å), at a scanning rate of 1 min^{-1} and in the scanning range from 20°–80°. Transmission electron microscope (TEM) images of the prepared nanoparticles are obtained with JEOL JEM 2010 transmission electron microscope operating at a voltage of 200 kV. The nanoparticles were drop coated over a carbon tape and further the samples were then sputter coated with platinum prior to their characterization using scanning electron microscopy (SEM, JEOL, Japan) to avoid charging effect. FTIR spectra were recorded using FTIR (CARRY 600Z series, Japan) to investigate the characteristics functional group of the samples. The Raman spectra of the samples were recorded using Raman spectrophotometer (STR-150 series, Japan) with Ar^+ laser of 532 nm excitation wavelength. LabIndia UV–Vis Spectrophotometer 3092 was used to obtain UV–Vis absorption spectra of pure and doped SnO_2 nanoparticles.

The thin films of biosynthesized Au-doped SnO_2 nanoparticles were tested for gas sensing. The electrical contacts of silver paste separated by 1 cm were coated on Au-doped SnO_2 thin films. The sensor was mounted in a stainless steel test chamber (volume: 250 cm^3). A desired concentration of the test gas in the chamber was achieved by injecting a known quantity of gas using a microsyringe. A change in resistance of the film as a function of time (response curve) was recorded at operating temperature of 200 C for 100, 60 and 20 ppm concentration of NO_2 gas, which was commercially procured. The response data was acquired by using a computer interfaced Keithley 2400 source meter. The recovery of the sensor was recorded by exposing the sensor to air. From the response curves, the response (S) was calculated using the relation:

$$S(\%) = R_g - R_a/R_a \times 100\% \quad (1)$$

where R_a and R_g are resistances in the air and test gas (NO_2), respectively [22–24]. Response and recovery times were defined as the time needed for 90% of total resistance change on exposure to gas and air, respectively.

3 Result and discussion

3.1 Structural characterization

3.1.1 X-ray diffraction (XRD)

Figure 2 represents the XRD pattern of (a) undoped SnO_2 and (b) Au-doped SnO_2 nanoparticles (Rietveld refined). The diffraction peaks of both the patterns in the spectra were indexed to the rutile phase of SnO_2 and the lattice parameters were calculated to a = 4.741 Å, c = 3.189 Å for pure SnO_2 and a = 4.742 Å, c = 3.189 Å for Au-doped SnO_2, which is consistent with the literature values (a = 4.738 Å, c = 3.186 Å, JCPDS No. 71–0652), belonging to the space group of P42/mnm.

In order to check the effect of strain on crystallite size, the crystallite size was calculated by Scherrer's formula and Williamson–Hall (W–H) plot as well. The differences of two sizes yield the required information. The crystallite size from Scherrer's formula, $D = 0.91\lambda/\beta \cos\theta$, where D is the crystallite size, λ is the wavelength of X-ray used, and θ is the Bragg angle of diffraction peaks. The variation of $\beta \cos\theta$ with $4\sin\theta$ gives the W–H plot from which the crystallite size D and lattice strain η can be calculated [25]. The results from both the methods show that the crystallite size increases with doping of Au. Due to Au doping, the system and lattice planes gets distorted, and thus the crystallite size increases. We can see a clear difference between sizes calculated by both the method and which is due to the lattice strain in the system. The positive strain implies an expansion in the system and hence doped system has higher W–H calculated crystallite size values compared to the crystallite sizes calculated by Scherer equation. No characteristic peak of Au was seen which indicates that no new phase of Au is created; it further confirms that the Au doping is due to chemical reaction mechanism and not due to diffusion [26, 27].

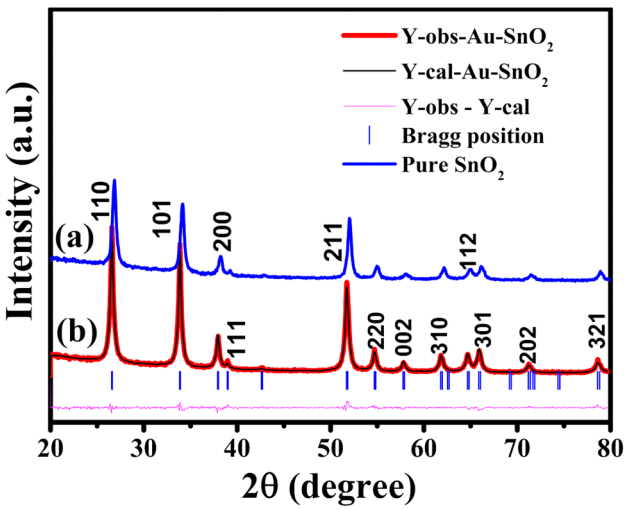

Fig. 2 XRD pattern of the (*a*) undoped SnO_2 and (*b*) (Rietveld refined) Au-doped SnO_2 nanoparticles

Also with Au doping, the peak positions slightly shift to the lower angles indicating a slight increase of the lattice parameter due to the strain on the lattice derived from the incorporation Au ions [28]. The ionic radius of Sn and Au in octahedral coordination is 0.69 and 0.85 Å, respectively [29], thus the Au ion prefers to occupy the Sn site. The ionic size of Au^{2+} being larger results in expansion of the system, which ultimately increases the positive strain listed as shown in Table S1. The interplanar spacing in pristine and Au 5 wt% doped SnO_2 nanosystem for 110 plane calculated from XRD is found to be 0.34 and 0.35 nm, respectively. To further confirm the crystal structure and lattice parameters of the pristine and Au-doped SnO_2, Rietveld refinement was performed. The results obtained are tabulated in Table S1. These results confirm the slight increase in lattice constants due to Au doping, which resulted in increased crystallite size and lattice strain.

3.2 Transmission electron microscopy (TEM)

Figure 3a shows the TEM image of 5% Au-doped SnO_2 and the inset shows the corresponding size distribution plot. TEM image confirms the prepared Au-doped SnO_2 nanoparticles to be in nano regime. No agglomeration of nanoparticles can be seen, which is very much as expected as the biomolecules present in the extract act as surfactants. The average crystallite size from TEM image of pristine SnO_2 reported in our previous work [21] was ~12 nm, while TEM image of Au-doped SnO_2 shows the clear formation of nanoparticles of ~25 nm. This confirms that doping of Au in SnO_2 has increased the particle size compared to pristine SnO_2. Furthermore in the TEM micrograph, we can clearly see no Au nanoparticle formation and or deposition on the surface of the SnO_2 nanoparticles, this is in good agreement with the XRD results which further confirms the doping mechanism.

3.3 Scanning electron microscopy (SEM)

The surface morphology of the biosynthesized Au-doped SnO_2 nanoparticles was examined by SEM. Figure 3b shows the micrograph of Au-doped SnO_2 nanoparticles calcined at 600 °C demonstrating spherical shaped nanoparticles with narrow size distribution. No major change in morphology of the Au-doped SnO_2 nanoparticles was observed when compared to pure SnO_2 [21].

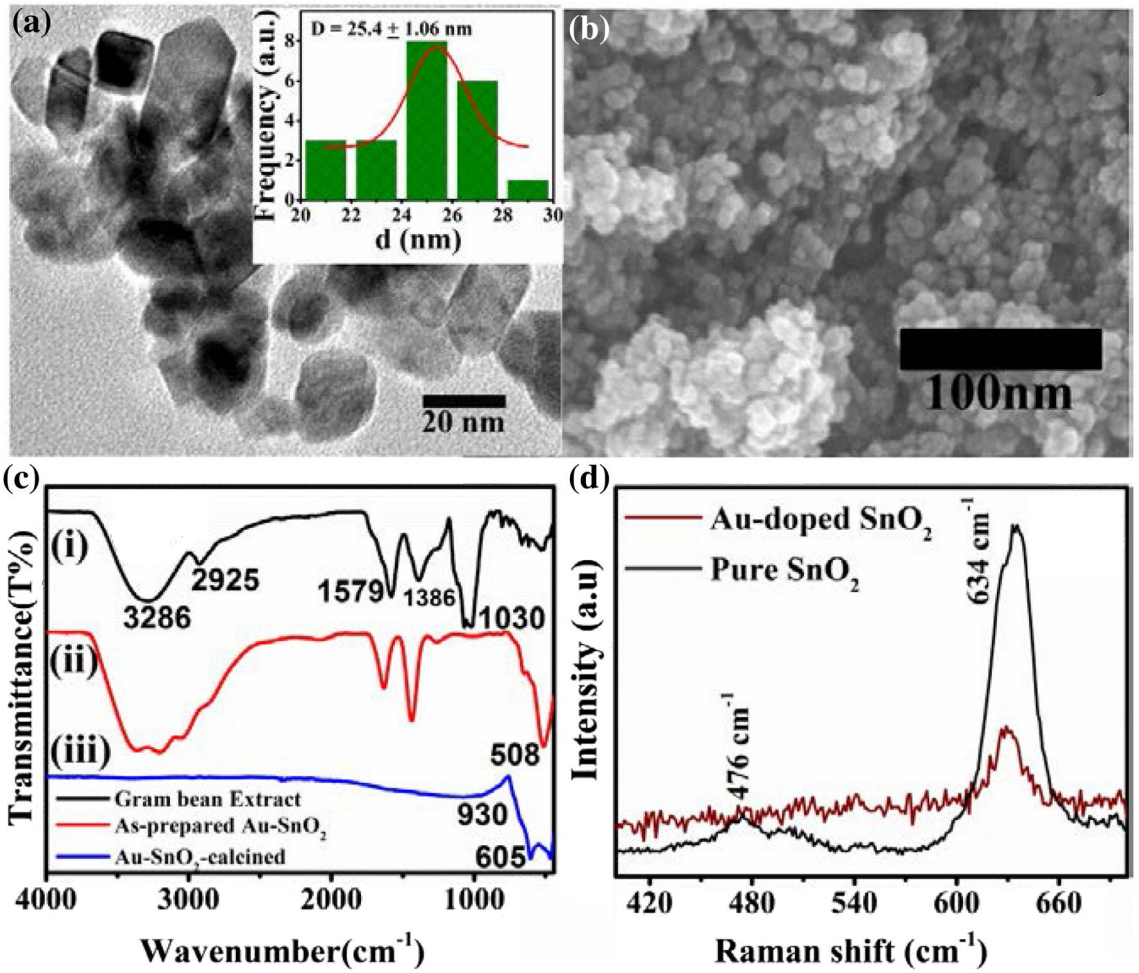

Fig. 3 **a** The TEM image (*inset*) size distribution histogram. **b** SEM image. **c** FTIR spectra of (*i*) gram bean extract (*ii*) as-prepared Au–SnO_2, (*iii*) Au-SnO_2 calcined at 600 °C. **d** Raman spectra of pure and Au-doped SnO_2 nanoparticles

3.3.1 Fourier transform infrared spectroscopy (FTIR)

Figure 3c shows the room temperature FTIR spectra of drop cast (i) gram bean extract, (ii) as prepared Au-doped SnO_2 and (iii) Au-doped SnO_2 calcined at 600 °C. The results are similar to our previous reports [21]. The biomolecule pectin present in the gram bean extract can be confirmed by the FTIR spectra. A typical IR absorption peak originating from stretching mode of the Sn–OH bond is found for the pectin–Au–SnO_2 composite sample at about 508 cm^{-1}; the remaining peaks in pectin–SnO_2 composite are induced by pectin, which is confirmed by comparing the IR spectrum of the composite with that of the pectin [30]. The peaks obtained and their corresponding modes are tabulated in Table S2.

The strong interactions between pectin and SnO_2 can be confirmed from the retention of pectin peaks even after repeated washing of the samples. The peaks at around 601 and 920 cm^{-1} refer to Sn–O stretching modes of Sn–O–Sn, which appear even after calcination at 600 °C. From the synthesis mechanism summarized in Fig. 1, we conclude that the pectin molecules are released in the extract due to autolysis of the cell walls when gram beans are soaked in de-ionised water [31, 32]. Pectin molecules have a tendency to bind metal ions [33], thus when tin chloride is added to the extract, the tin ions get bound to the pectin molecules as shown in Fig. 1. Tin-hydroxide-pectin gel shrinks [20] as the pH of the solution is increased and this inhibits the further growth of the nanoparticles. Subsequently, after calcination of the sample, we get very small-sized nanoparticles with narrow size distribution.

3.4 Raman spectroscopy

Raman spectroscopy is an effective tool to study the structural and vibrational properties of a material. The Au-doped SnO_2 samples were investigated using Raman spectroscopy to confirm the substitution of Au ions in SnO_2 lattice and to

understand its effect on vibrational properties. The Raman spectra for pure and Au-doped SnO_2 sample is shown in Fig. 3d. A normal mode can be described by the 3 n coordinates, where n is the number of atoms in the primitive cell. This gives the displacements of the atoms from their equilibrium positions [34]. Rutile SnO_2 having six atoms unit cell gives out 18 possible vibrations. The normal lattice vibrations at the Γ point of the Brillouin zone on the basis of group theory are as follows [35]:

$$\Gamma = \Gamma_1^+(A_{1g}) + \Gamma_2^+(A_{2g}) + \Gamma_3^+(B_{1g}) + \Gamma_4^+(B_{2g}) + \Gamma_5^-(E_g) + 2\Gamma_1^-(A_{2u}) + 2\Gamma_4^-(B_{1u}) + 4\Gamma_5^+(E_u) \quad (2)$$

From the Raman spectra, we can clearly see that the pure SnO_2 exhibits the obvious A_{1g} mode at 634 cm^{-1} and Eg mode at 476 cm^{-1} but the intensity of A_{1g} mode gets reduced with the 5 wt% Au doping. The reduction in the intensity of A_{1g} mode can be attributed to the lattice distortion due to the substitution of Au at the Sn site [36]. Along with the distortion, generation of oxygen vacancies is another possible reason for the reduction of the peak intensity [37]. The substitution of the metal ions in the lattice is reported to weaken the metal oxygen bond in the SnO_2 lattice. Choudhary et al. [38] reported increased reactivity of the lattice oxygen due to the doping of metals. This increase in the reactivity of the lattice oxygen was surmised to be due to the creation of crystal defects and an increase in the mobility of lattice oxygen [39].

3.5 UV–Vis spectroscopy

Absorption spectroscopy is a powerful non-destructive technique to have a better understanding of the effect of Au doping on optical properties of semiconducting nanoparticles. The absorption spectra of pure and Au-doped SnO_2 nanoparticles are shown in Fig. 4a. The absorbance is expected to depend on several factors such as band gap, oxygen deficiency, surface roughness and impurity centers. Absorbance spectra show an ultraviolet cut-off around 250–290 nm, which can be attributed to the photoexcitation of electrons from valence band to conduction band. The bandgap of the pure and Au-doped nanoparticle thin films was calculated by extrapolating the plot of $(\alpha h\nu)^2$ versus $h\nu$ using the Tauc's relation. The prepared pristine SnO_2 has a band gap of 3.54 eV, while its band gap slightly increases to 3.56 eV with the Au doping. Similar results were also observed for Au-doped SnO_2 synthesized by magnetron reactive sputtering [40]. Urbach type absorption is the absorption below band gap (inset Fig. 4b). When defects in the system increase then the below band absorption occurs. With Au doping the Urbach energy increases, which mean that the distortion increases [41].

The inset in Fig. 4a shows the higher absorption in near infra-red region. This peak is due to the d–d transition of electrons in Au ion. The transition takes place from ground state ^2Eg to excited state $^2T_{2g}$ of Au in octahedral coordination [42].

3.6 Gas sensing

Gas-sensing behaviors of the biosynthesized Au-doped SnO_2 sensor were explored after gas injection. Figure 5a shows the response curves for different gas concentrations of NO_2 at 200 °C temperature. The response curve shows

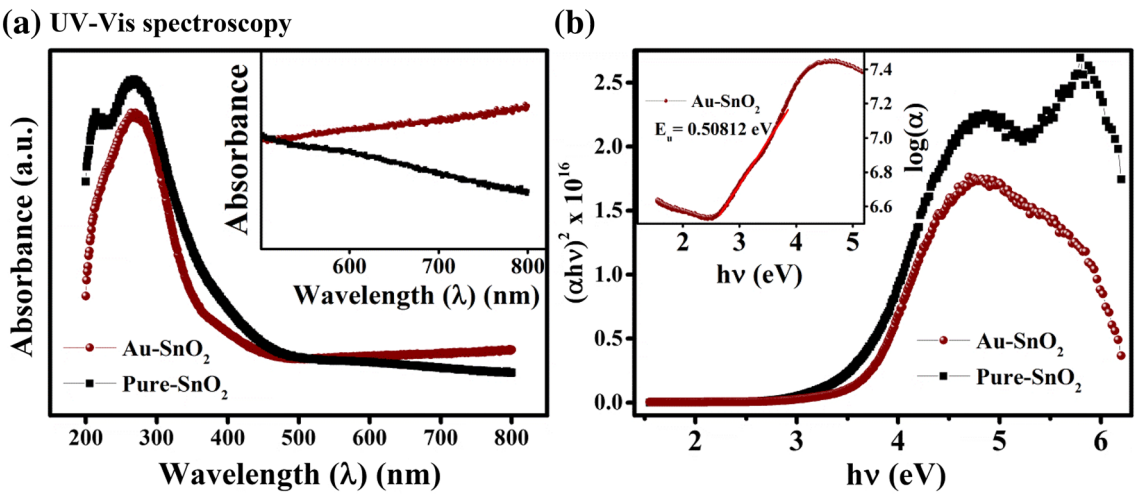

Fig. 4 **a** Absorbance spectra and **b** $(\alpha h\nu)^2$ vs $h\nu$ plot of pure and Au-doped SnO_2 nanoparticles

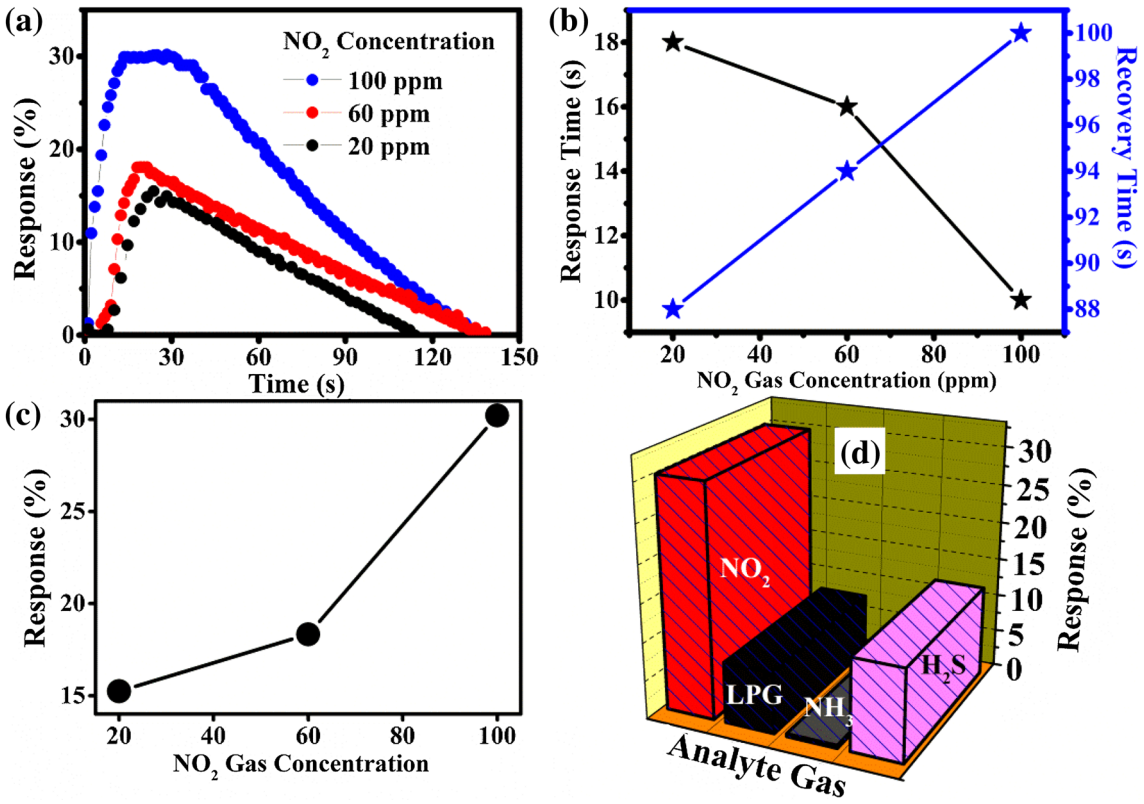

Fig. 5 **a** Response curves for varying gas concentrations, **b** sensor response and recovery time versus NO_2 gas concentration, **c** sensor response vs NO_2 gas concentration and **d** gas selectivity of the Au-doped SnO_2 sensor

linear increase in response with increase in gas concentration. Figure 5b shows the response and recovery time as a function of gas concentration. The response time is observed to decrease with increasing gas concentration while the recovery time increases. This may be due to the heavier nature of NO_2 and the reaction products which delay the desorption of the gas and species from the interface after the interaction, resulting in a decrease in desorption rate [43]. Figure 5c shows gas response versus gas concentration plot which also shows a linear increase in response to increasing NO_2 gas concentration. A response of 30.21% is obtained at 100 ppm. Table 1. shows the comparison of gas-sensing characteristics of Au-doped SnO_2 sensing material in the present work and those reported in the literature. The biomaterials used for synthesis are used either as templates or as binders. The use of biomaterials such as butterfly wings restricts their large scale industrial use, whereas the bio-green synthesis method reported in this work gives promising results with suitability for large-scale industrial production.

It is well known that the NO_2 sensing mechanism of SnO_2 depends on the surface oxygen adsorbed on the SnO_2 nanoparticles surface. The sensing mechanism involving adsorption of oxygen species on the surface of tin oxide nanoparticles abstract electrons, and thus, cause an increase in the potential barrier at the grain boundaries. The gas molecules interact with the oxygen species and produce a notable change in the electronic property

Table 1 Comparison of gas-sensing characteristics of biosynthesized Au–SnO_2 in present work and those reported in the literature

Sr. no	Sensing material	Biomaterial	Analyte gas	Gas conc.	Response	Ref. no.
1	Quasi-honeycomb like Fe_2O_3	Papilio Paris butterfly wings	NO_2	50 ppm	~5	[44]
2	A gold-binding M13 bacteriophage	M13 bacteriophage	NO_2	0.5 ppm	~5	[45]
3	Co_3O_4–carbon hybrids	Trogonoptera Brookiana butterfly wings	NO_2	100 ppm	14.7	[46]
4	Ni–CoOOH	Morpho butterfly wings	NO_2	100 ppm	~1	[47]
5	Au–SnO_2 nanoparticles	Gram bean extract mediated synthesis	NO_2	100 ppm	~30	This work

of the material. Thus, the density of oxygen species on the surface defines the rate of reaction and catalytic property. NO_2 is an oxidizing gas with electron affinity much higher than oxygen (0.48 eV). Thus, NO_2 can interact with SnO_2 by trapping electrons directly through the surface oxygen ions thereby forming new surface electron acceptor levels [48, 49].

The interaction of pre-adsorbed oxygen and NO_2 molecules on the surface of SnO_2 is indicated in Eqs:

$$O_2 gas \xrightarrow{Au-SnO_2+\ air} O_2(ads) \quad (3)$$

$$O_2(ads) + e^- \xrightarrow{Au-SnO_2+\ air} O_2^-(ads) \quad (4)$$

$$O_2^-(ads) + e^- \xrightarrow{Au-SnO_2+\ air} 2O^-(ads) \quad (5)$$

$$NO_2(gas) \leftrightarrow NO_2(ads) \quad (6)$$

$$NO_2(ads) + O_2^-(ads) + 2e^- \leftrightarrow NO_2^-(ads) + 2O^-(ads) \quad (7)$$

These series of reactions result in the further decrease in concentration of electrons on the surface of SnO_2, which lead to the increase in resistivity of the material. This change in resistivity can be used for the detection of NO_2. There are many reports [16, 50–54] for enhanced gas sensing behaviors of SnO_2 nanoparticles decorated with Au nanoparticles and the mechanism is explained by "spill-over effect", meaning that the Au particles enhance the surface of the active metal oxide with oxygen species. However, the Au-doped SnO_2 nanoparticles in this work showed no evidence of forming metallic particles either at the surface or in the interior of SnO_2 nanoparticles. This is confirmed by the TEM results. On the basis of the TEM observations and the previous report [55], the first principle calculations for the formation energies of Au dopants in SnO_2 reveals that Au prefers the substitutional site. Thus, in the present case, the enhancement in response is supposed to be explained by the structural defects generated due to the incorporation of the Au ions in the SnO_2 lattice. Along with this, acceptor-compensated charge transport mechanism is supposed to be responsible for the enhanced gas sensing behavior [55]. Selectivity is another important sensor parameter. The responses of Au-doped SnO_2 sensors towards a variety of gasses including NO_2, H_2S, LPG, and NH_3 of 100 ppm at 200 °C temperature were explored to evaluate their selectivity. Figure 5d shows that the gas sensor of 'Au-doped SnO_2' exhibits excellent selectivity to NO_2 gas when compared to other gasses. The results suggest that the Au-doped SnO_2 thin film sensor can be fabricated to monitor NO_2 gas from the polluted air. In summary, the NO_2 sensing performances of SnO_2 nanoparticle thin film were improved greatly by Au doping. This study provides novel insights as well as aids the development of next-generation green chemical sensors.

4 Conclusion

In this work, well dispersed Au-doped SnO_2 nanoparticles with narrow size distribution with size ~25 nm were successfully biosynthesized using remnant water (ideally kitchen waste) collected from soaked Bengal gram beans (*C. arietinum* L.). XRD and Raman measurement confirm the doping of Au which replaces Sn^{4+} from the system. UV–Vis spectra supported the results showing a slight increase in bandgap with Au doping. Gas sensor based on the Au-doped SnO_2 showed the gas response of ~30% for 100 ppm of NO_2 gas, which is a promising result for the biosynthesized Au-doped SnO_2 nanoparticles thin film for gas sensing application. This response can be attributed to the lattice distortion induced by Au doping and also the oxygen vacancies generated therein. It is concluded that the structural modifications and defect generation due Au-doping in SnO_2 lattice plays an important role in enhancing the response and increases the selectivity for NO_2 gas.

Acknowledgements The authors are thankful to UGC-DAE Consortium for Scientific Research, Indore (Project Ref. No: CSR-I/CRS-48/48) and UGC, New Delhi (F. No. 41–370/2012 (SR)) for the financial support. We are also thankful to the Department of Nanotechnology, Dr. B. A. M. University and Department of Chemistry, Shivaji University, Kolhapur for providing the laboratory facility.

References

1. USEP Agency (2016), https://www.epa.gov/no2-pollution
2. J.-R. Zhang, L. Gao, L.-X. Gu, Chin. J. Inorg. Chem. **22**, 2001–2004 (2006)
3. M.G. Ghozikali, M. Mosaferi, G.H. Safari, J. Jaafari, Environ. Sci. Pollut. Res. **22**, 2817–2823 (2015)
4. R Jain, Y. Lei, R. Maric, Sens. Actuators B **236**, 163–172 (2016)
5. J.R. Liang, W.J. Li, J.F. Liu, M. Hu, J. Alloys Compd. **687**, 845–854 (2016)
6. YLT Ngo, S.H. Hur, Mater. Res. Bull. **84**, 168–176 (2016)
7. A. Stanoiu, S. Somacescu, J.M. Calderon-Moreno et al., Sens. Actuators B **231**, 166–174 (2016)
8. S. Cao, W. Zeng, H. Zhang, Y. Li, J. Mater. Sci. **26**, 2871–2878 (2015)
9. N. Zhao, Z. Chen, W. Zeng, J. Mater. Sci. **26**, 9152–9157 (2015)
10. I.H. Kadhim, H.A. Hassan, J. Mater. Sci. **27**, 4356–4362 (2016)
11. M. Gardon, J.M. Guilemany, J. Mater. Sci. **24**, 1410–1421 (2013)
12. A. Yildiz, A.A. Alsaç, T. Serin, N. Serin, J. Mater. Sci. **22**, 872–875 (2011)
13. G. Sakai, N. Matsunaga, K. Shimanoe, N. Yamazoe, Sens. Actuators B **80**, 125–131 (2001)
14. Z. Li, X. Wang, T. Lin, J. Mater. Chem. A **2**, 13655–13660 (2014)
15. H. Xia, Y. Wang, F. Kong et al., Sens. Actuators B **134**, 133–139 (2008)

16. J. Zhang, X. Liu, S. Wu, M. Xu, X. Guo, S. Wang, J. Mater. Chem. **20**, 6453–6459 (2010)
17. X. Liu, J. Zhang, L. Wang et al., J. Mater. Chem. **21**, 349–356 (2011)
18. R.K. Joshi, Q. Hu, F. Alvi, N. Joshi, A. Kumar, J. Phys. Chem. C **113**, 16199–16202 (2009)
19. Wikipedia Pectin, https://en.wikipedia.org/w/index.php?title=Pectin&oldid=674518015
20. T.F. Vandamme, A. Lenourry, C. Charrueau, J. Chaumeil, Carbohydr. Polym. **48**, 219–231 (2002)
21. K.P. Gattu, K. Ghule, A.A. Kashale et al., RSC Adv. **5**, 72849–72856 (2015)
22. G.D. Khuspe, S.T. Navale, D.K. Bandgar, R.D. Sakhare, M.A. Chougule, V.B. Patil, Electron. Mater. Lett. **10**, 191–197 (2014)
23. MA Chougule, SR Nalage, S Sen, VB Patil, J. Exp. Nanosci. **9**, 482–490 (2012)
24. S.T. Navale, A.T. Mane, M.A. Chougule, N.M. Shinde, J. Kim, V.B. Patil, RSC Adv. **4**, 44547–44554 (2014)
25. A.K. Zak, W.H. Abd. Majid, M.E. Abrishami, R. Yousefi, Solid State Sci. **13**, 251–256 (2011)
26. G.N. Advani, Y. Komem, J. Hasenkopf, A.G. Jordan, Sens. Actuators B **2**, 139–147 (1981)
27. S.D. Bakrania, M.S. Wooldridge, Sensors **10**, 7002–7017 (2010)
28. G. Qin, F. Gao, Q. Jiang et al., Phys. Chem. Chem. Phys. **18**, 5537–5549 (2016)
29. R. Shannon Acta Crystallogr. Sect. A **32**, 751–767 (1976)
30. L. Shi, S. Gunasekaran, Nanoscale Res. Lett **3**, 491–495 (2008)
31. E. Martinez-Manrique, C. Jacinto-Hernandez, R. Garza-Garcia, A. Campos, E. Moreno, I. Bernal-Lugo, J. Sci. Food. Agric. **91**, 2394–2398 (2011)
32. J.M. Sevillano, I. Zarra, J.L. Acebes, Plant Cell Physiol. **38**, 1259–1263 (1997)
33. B.A. McKenna, T.M. Nicholson, J.B. Wehr, N.W. Menzies, Carbohydr. Res. **345**, 1174–1179 (2010)
34. R.S. Katiyar, J. Phys. C **3**, 1087–1096 (1970)
35. A. Diéguez, A. Romano-Rodríguez, A. Vilà, J.R. Morante, J. Appl. Phys. **90**, 1550–1557 (2001)
36. P. Chetri, B. Saikia, A. Choudhury, J. Appl. Phys. **113**, 233514–233518 (2013)
37. V. Agrahari, M.C. Mathpal, S. Kumar, M. Kumar, A. Agarwal, J. Mater. Sci. **27**, 6020–6029 (2016)
38. V.R. Choudhary, B.S. Uphade, S.G. Pataskar, A. Keshavaraja, Angew. Chem. Int. Ed. **35**, 2393–2395 (1996)
39. J.L.G. Fierro, *Metal Oxides: Chemistry and Applications* (CRC Press, Boca Raton, 2005)
40. A.S. Reddy, N.M. Figueiredo, A. Cavaleiro, Vacuum **86**, 1323–1327 (2012)
41. P. Chetri, A. Choudhury, Phys. E **47**, 257–263 (2013)
42. D.N. Sathyanarayana, *Electronic Absorption Spectroscopy and Related Techniques* (Universities Press, 2001)
43. GD Khuspe, RD Sakhare, ST Navale et al., Ceram. Int. **39**, 8673–8679 (2013)
44. W.H. Peng, C.L. Zhu, S.M. Zhu, F. Yao, Y. Li, D. Zhang, J. Mater. Sci. **48**, 4336–4344 (2013)
45. C.H. Moon, M. Zhang, N.V. Myung, E.D. Haberer, Nanotechnology **25**, 135205 (2014)
46. J.J. Zhang, Y.Q. Liang, J. Mao et al., Sens. Actuators B **235**, 420–431 (2016)
47. C.L. Kuo, J.W. Wang, Y.M. Kuo, Fresenius Environ. Bull. **25**, 2977–2984 (2016)
48. B. Ruhland, T. Becker, G. Müller, Sens. Actuators B **50**, 85–94 (1998)
49. M. Epifani, J.D. Prades, E. Comini et al., J. Phys. Chem. C **112**, 19540–19546 (2008)
50. L.H. Qian, K. Wang, Y. Li, H.T. Fang, Q.H. Lu, X.L. Ma, Mater. Chem. Phys. **100**, 82–84 (2006)
51. X.Z. Wang, S. Qiu, C.Z. He, G.X. Lu, W. Liu, J.R. Liu, RSC Adv. **3**, 19002–19008 (2013)
52. S.J. Choi, M.P. Kim, S.J. Lee, B.J. Kim, I.D. Kim, Nanoscale **6**, 11898–11903 (2014)
53. J.H. Kim, Y. Zheng, A. Mirzaei, S.S. Kim, Korean. J. Mater. Res. **26**, 741–750 (2016)
54. Y. Li, F.X. Zhao, X.X. Lian, Y.L. Zou, Q. Wang, Q.J. Zhou, J. Electron. Mater. **45**, 3149–3156 (2016)
55. A. Katoch, G.J. Sun, S.W. Choi et al., Sci. Rep. **4**, 4622 (2014)